Chemistry
A European
Journal

Chemistry Europe
European Chemical Societies Publishing

Accepted Article

Title: Evidence for multiple binding modes in the initial contact between SARS-CoV-2 spike S1 protein and cell surface glycans

Authors: Michela Parafioriti, Minghong Ni, Maurice Petitou, Courtney J. Mycroft-West, Timothy R. Rudd, Neha S. Gandhi, Vito Ferro, Jeremy E. Turnbull, Marcelo A. Lima, Mark A. Skidmore, David G. Fernig, Edwin A. Yates, Antonella Bisio, Marco Guerrini, and Stefano Elli

To be cited as: *Chem. Eur. J.* **2022**, e202202599

Link to VoR: https://doi.org/10.1002/chem.202202599

WILEY-VCH

10.1002/chem.202202599

WILEY-VCH

RESEARCH ARTICLE

Evidence for multiple binding modes in the initial contact between SARS-CoV-2 spike S1 protein and cell surface glycans

Michela Parafioriti,[a] Minghong Ni,[a] Maurice Petitou,[a] Courtney J. Mycroft-West,[b] Timothy R. Rudd,[c, g] Neha S. Gandhi,[d] Vito Ferro,[e] Jeremy E. Turnbull,[f, g] Marcelo A. Lima,[f] Mark A. Skidmore,[f, g] David G. Fernig,[g] Edwin A. Yates,[g, f] Antonella Bisio,[a] Marco Guerrini *[a] and Stefano Elli *[a]

Dedication: dedicated to Prof. Benito Casu

[a] Dr, MP, Parafioriti; Dr, MN, Ni; Dr, MP, Petitou; Ph.D. AB, Bisio; Dr. MG, Guerrini*; Ph.D, SE, Elli*
Department NMR and Carbohydrates
Istituto di Ricerche Chimiche e Biochimiche 'G. Ronzoni'
via Giuseppe Colombo 81, 20133 Milano, Italy
E-mail: elli@ronzoni.it, guerrini@ronzoni.it
[b] Ph.D, CJM, Mycroft-West
Structural Biology
Rosalind Franklin Institute
Harwell Campus, Didcot, OX11 0QS, United Kingdom
[c] Ph.D., TRR, Rudd
Analytical and Biological Sciences Division
National Institute for Biological Standards and Control
Potters Bar, Hertfordshire, United Kingdom
[d] Ph.D., NSG, Gandhi
School of Chemistry and Physics, Queensland University of Technology; Centre for Genomics and Personalised Health, Queensland University of Technology
2 George St, Brisbane, QLD-4000, Australia; Brisbane, Australia
[e] Prof. VF, Ferro
School of Chemistry and Molecular Biosciences; Australian Infectious Diseases Research Centre
The University of Queensland, Brisbane, Australia
[f] Prof. JET, Turnbull; PhD, MAL, Lima; PhD, MAS, Skidmore; PhD, EAY, Yates; Ph.D.
Centre for Glycoscience, Keele University
Newcastle-Under-Lyme, Staffordshire, ST5 5BG, United Kingdom
[g] Ph.D., TRR, Rudd; Ph.D.; DGF, Fernig; Prof. JET, Turnbull; Ph.D., EAY, Yates; Ph.D.
Department of Biochemistry and Systems Biology, Institute of Systems, Molecular and Integrative Biology, University of Liverpool
Liverpool, L69 7ZB United Kingdom

Supporting information for this article is given via a link at the end of the document.

Abstract: Infection of host cells by SARS-CoV-2 begins with recognition by the virus S (spike) protein of cell surface heparan sulfate (HS), tethering the virus to the extracellular matrix environment, and causing the subunit S1-RBD to undergo a conformational change into the 'open' conformation. These two events promote the binding of S1-RBD to the angiotensin converting enzyme 2 (ACE2) receptor, a preliminary step toward viral-cell membrane fusion. Combining ligand-based NMR spectroscopy with molecular dynamics, oligosaccharide analogues were used to explore the interactions between S1-RBD of SARS CoV-2 and HS, revealing several low-specificity binding modes and previously unidentified potential sites for the binding of extended HS polysaccharide chains. The evidence for multiple binding modes also suggest that highly specific inhibitors will not be optimal against protein S but, rather, diverse HS-based structures, characterized by high affinity and including multi-valent compounds, may be required.

Introduction

The severe acute respiratory syndrome coronavirus-2 (SARS-CoV-2, a betacoronavirus[1, 2]) spread rapidly from the Wuhan region of China to Europe in early 2020 and worldwide soon after, and was responsible for the highly contagious coronavirus disease (COVID-19). COVID-19 is characterized by a broad spectrum of severity, initially affecting the respiratory tract, where it is known to cause interstitial pneumonia and acute respiratory distress syndrome (ARDS). In addition, COVID-19 can induce hyper-inflammation which, combined with hypoxia, immobilisation, and diffuse intravascular coagulation (DIC), renders patients susceptible to both venous and arterial thromboembolic disease [3, 4], symptoms that can extend in many patients beyond the infection giving rise to 'Long Covid' [5]. The efficacy of vaccines administered since 2021 is not complete and variants of different immunogenicity arise regularly. Thus, improved understanding of the molecular aspects of the early stage of the infection is fundamental to enabling the design of new antiviral drugs including inhibitors for both disease treatment and prophylaxis.

Infection is initiated by the interaction of the virus glycoprotein S (spike protein) with its cell surface receptor systems. The major, but by no means sole, system consists of the angiotensin converting enzyme 2 (ACE2) receptor and the polysaccharide heparan sulfate (HS) co-receptor. The S protein is a homotrimer, whose structure is divided in two subunits, S1 and S2, and it is the former that contains the receptor-binding domain (S1-RBD),

10.1002/chem.202202599

corresponding to the subunit of the S protein that specifically binds ACE2. S1-RBD is by default in the 'down' conformation where the ACE2 recognition interface is hidden in the S1, preventing its interaction with this receptor, [6, 7] and avoiding its contact with the immune system. Binding to the HS co-receptor drives the conformational change of S1-RBD to the 'up' conformation, which exposes the ACE2 recognition interface of the S1 RBD, enabling it to bind ACE2. [8-12] The involvement of HS as a co-receptor mirrors other coronaviruses, including murine coronavirus [13] and human coronavirus CoV-NL63 [14] and has parallels with the many HS-dependent growth factors, which have an analogous dual receptor system. [14]

Since the first demonstration of binding and conformational change induced in S1-RBD by heparin, [16] a considerable effort has gone into defining the molecular 'keys' underpinning this interaction. Heparin, a proxy for HS was observed to promote the 'down' to 'up' conformational change in the S1-RBD and cell infectivity by SARS-CoV-2, [12, 17] while, progress has been made in identifying potential HS binding sites on S1-RBD [17, 18] and potential saccharide structures in HS that engage the S protein [18-24]. These results, while hinting at apparent high specificity and selectivity of S1 RBD for HS, more likely represent a correspondence between high charge and binding, a property that is commonly observed among HS-protein interactions, when heparin is used as an experimental proxy. Thus, there remains a considerable gap in our understanding of the atomic basis of the interaction of S1-RBD and, indeed, S1 with HS, despite this interaction providing an opportunity for the development of treatments and prophylaxis.

In the present study we have used a combination of saturation transfer difference NMR (STD NMR) and synthetic models: hexasaccharide MeO-(4)-α-L-IdoA2S(1→4) α-D-GlcNS,6S (1→4) β-D-GlcA(1→4) α-D-GlcNS,6S (1→4) α-L-IdoA2S α-D-GlcNS,6S(1)-OMe: **(1)**, pentasaccharide, α-D-GlcNS,6S (1→4) β-D-GlcA (1→4) α-D-GlcNS,3S,6S (1→4) α-L-IdoA2S (1→4) α-D-GlcNS,6S α(1)-OMe: **(2)**, and nonasaccharide β-D-GlcA (1→4) α-D-GlcNS,6S (1→4) β-D-GlcA (1→4) α-D-GlcNS,3S,6S (1→4) α-L-IdoA2S (1→4) α-D-GlcNS,6S (1→4) α-L-IdoA2S (1→4) α-D-GlcNS,6S (1→4) β-D-GlcA-pPhNO$_2$ **(3)**, whose sequences are depicted in ~~(~~**Scheme 1**~~)~~, to probe interaction of sugars with the S1-RBD (Wuhan strain). Ligand-based NMR spectroscopy, which provides experimental evidence for the location of interactions within molecules and changes in their conformation on binding, was combined with theoretical methods to enable a model of the interaction to be constructed and tested against the experimental measurements. The results support the idea that the interaction between HS and S1-RBD is characterised by low specificity and probable low selectivity, highlighting the role of extracellular HS as the initial, dynamic contact that enables subsequent binding of the S protein to the ACE2 receptor. This knowledge has implications for our understanding of the natural history of the disease and will influence strategies for the design of potential inhibitors of SARS-CoV-2 viral binding.

Results

The interaction between the target host cell and SARS-CoV-2 is mediated by the glycoprotein S (spike), possessing an inverted-conical shape, externally decorating the viral membrane [25- 28] and provides the virus capsid with its characteristic 'crown' morphology. The S1 subunit is characterized by a triangular section (C3 axial symmetry), that protrudes from the virus capsid, allowing it to bind the host cell. The S2 subunit includes part of the cylindrical stem connecting the distal S1 to its intra-membrane domain and drives the fusion process between the viral and cellular membranes [27]. The S1 subunit includes the N-terminal domain of the S protein and the receptor binding domain (S1-RBD), the latter presenting a β-sandwich structure decorated with loops and corresponding to the 'forefront' of the coronavirus. The S1-RBD is characterized by a hinge providing a degree of freedom that allows it to lift from the plane of the S1 trimer, assuming an 'up' instead of a 'down' conformation (**Figure 1**). [29] Here, the interactions were first characterized by ^{1}H NMR saturation transferred difference spectra (^{1}H-STD NMR) using **(1)**, **(2),** and **(3)** as ligand probes, and by comparing NOEs and transferred NOEs (trNOEs) using **(1)**. A hybrid docking and molecular dynamics (MD) simulation procedure was first employed to define the binding site on the S1-RBD surface. In a second step, 3D models of saccharide-S1-RBD complexes were constructed and validated, comparing simulated complete relaxation and conformational energy matrix analysis (CORCEMA) and experimental intra-residue and inter-glycosidic trNOEs. For the interaction of hexasaccharide **(1)**, at least two geometries, characterized by distinct modes of ligand-receptor binding, were required to interpret the experimentally observed trNOEs. Analogously, theoretical methods supported by ^{1}H-STD NMR indicated that pentasaccharide **(2)** also binds S1-RBD in both modes, while only a limited portion of nonasaccharide **(3)** contiguously binds S1-RBD, suggesting a recognition site on the surface of S1-RBD of fewer than six sugar residues.

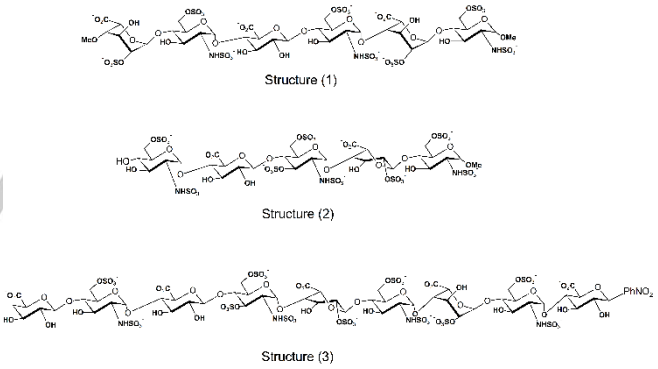

Scheme 1. Hexasaccharide **(1)**, pentasaccharide **(2)**, and nonasaccharide **(3)** used as ligand probes. These sequence representations depict the sugar residues in their most prevalent conformations in the unbound state; in the case of L-IdoA2S residues, this can be either $^1C_4$ or $^2S_0$ depending on the sulfation degree of the neighbouring glucosamines (see text).

*NMR characterization of oligosaccharides **(1)**, **(2)** and **(3)**.* The NMR spectrum of **(1)** was first recorded in solution to enable comparison with protein-bound forms. The proton spectrum of **(1)** is shown in **Figure 2** (black line) with assignments (**Table S2a)**, and spectra (**Figure S3a)**. NMR characterization of heparin pentasaccharide **(2)** has been published. [30, 31] The nonasaccharide **(3)** follows the same NMR characterization as **(1)**, here summarized by the ^{1}H-^{13}C HSQC spectrum (**Figure S3b)**.

*Identification of the groups involved in interactions between oligosaccharide **(1)**, **(2)**, **(3)** and S1-RBD by NMR spectroscopy.*

10.1002/chem.202202599

Interaction between oligosaccharide ligand **(1)** and proteins can be monitored qualitatively from changes to chemical shift and linewidth ^{1}H NMR signals. Increasing linewidths and the absence of altered chemical shifts are consistent with an equilibrium regulated by intermediate rates of exchange between the free and bound state (**Figure 2**). The estimated K_d for the interaction of **(1)**-S1-RBD is 4.5 10^{-7} M (Materials and Methods).

The regions of **(1)** involved in binding were determined by ^{1}H-STD NMR spectroscopy; the portion of the ligand showing the shortest distances to the protein surface exhibiting the most intense NMR signals. In oligosaccharide **(1)** the IdoA2S residue at the non-reducing end (residue F) had the lowest ^{1}H-STD NMR signals indicating generally longer distances from the protein surface compared to other residues, which showed high or medium intensity STD NMR signals (70% to 100%), indicating their proximity to the protein surface (**Figures 3 a**, **b**). As a comparison, the binding epitope of **(2)** for its interaction with S1-RBD and the corresponding partial ^{1}H-STD NMR spectrum (**Figure 3 c** and **d**) shows that, except for GlcNS6S (residue E) and IdoA2S (residue B), whose intensities are between 40 and 70%, all the residues of **(2)** exhibit high intensity signals for H1 (70-100%). Moreover, the STD NMR spectrum of **(3)** suggest that only an hexasaccharide portion of this glycan is in close contact with the protein. In fact, weaker STD NMR signals were observed for the anomeric protons of the reducing IdoA2S- GlcNS,6S disaccharide (residues B, A) as well as the non-reducing unsaturated GlcA (residue I), (**Figure 3 e**, **f**). The intensities of the ^{1}H-STD NMR spectra in **Figure 3 b**, **d and f** are reported in **Table S1**. It is interesting to observe that the small amount of trehalose (protein preservative), present in all reference spectra (**Figure 3**, black line), is totally absent in the corresponding STD spectra. This demonstrates the effectiveness of the STD experiments in discriminating between interacting (HS oligosaccharides) and non-interacting molecules.

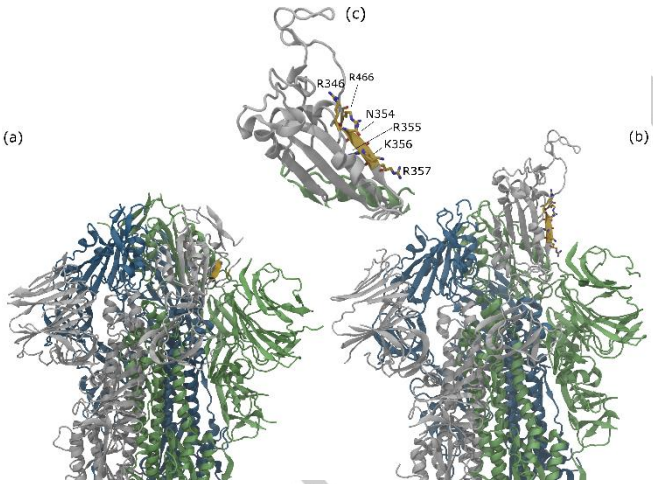

Figure 1. Protein S reported in closed (a) and in open (b) states. The S1 subunit of the protein S are depicted in a ribbon representation; the three monomers of the protein S are highlighted as blue, green, and grey ribbons. The 3D structures of the protein S in closed and open forms derive from cryo-EM models, 6VXX [28] and 6VYB [28], respectively. The receptor binding domain (S1-RBD) in the grey monomer is reported in the closed state (a) and in the open state (b) respectively; for the latter, the higher resolution structure (X-ray model, PDB ID 6M0J [9]) was superimposed on the sequence (333 to 526) of the model 6VYB (chain B, grey ribbon; final RMSD 0.72 Å). The key residues R346, N354, R355, K356, R357 and R466 of the S1-RBD (chain B) are highlighted in orange ribbon in the closed state and by both orange ribbon and tubes in the open state, respectively (see the zoomed-in view of the S1-RBD in panel (c).

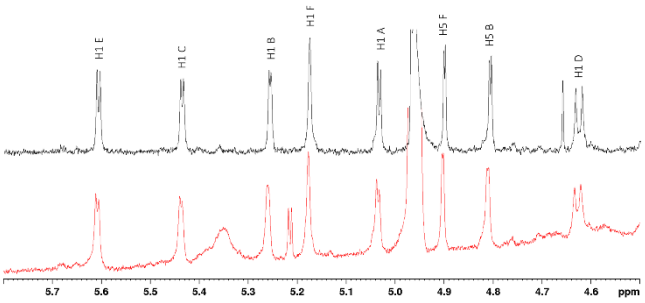

Figure 2. ^{1}H NMR signal broadening indicates interactions between hexasaccharide (1) and S1-RBD in the region 4.6 - 5.6 ppm, in which signals predominantly from the anomeric (H1) positions of the sugar residues fall, unimpeded by other signals. ^{1}H NMR spectra of **(1)** unbound (upper, black) and in the presence of S1-RBD (lower, red) in a 7 to 1 ratio. ^{1}H NMR spectra were acquired in D_2O.

Table 1. Summary of molecular docking/MD simulation for the estimated binding energy of **(1)**-S1-RBD, examining sites I, II, and III. [17] Each cluster corresponds to a docking solution and is represented by the complex geometry with the lowest binding energy. (ADT: autodock score function, 2nd column); cluster population (3rd column); estimated error on ΔG_{PB}^{bind} in brackets, last digit; MD simulation relaxation times (4th column); interval for the energy estimation (5th column); selected docking solutions were submitted to MD simulation to estimate the Poisson Boltzman free energy of binding ΔG_{PB}^{bind} (6th column)

Cluster Rank	ADT Lowest binding energy[a]	Cluster Population	MD simulation Relaxation time[b]	Average time interval [b]	ΔG_{PB}^{bind} [a]
Site I					
1	-2.50	3	80	[80,100]	-30.6(3)
2	-1.70	2	36	[36, 56]	-32.3(6)
3	-1.33	2	36	[36, 56]	-30.6(4)
Site II					
1	0.26	2	36	[36, 56]	-9.7(4)
2	1.12	7	58	[58, 78]	-10.4(5)
Site III					
1	0.10	4	40	[40, 60]	-12.1(3)
2	1.23	3	52	[52, 72]	-6.7 (3)

[a] Energy is Kcal mol^{-1}. [b] Simulation time is in nanoseconds (ns).

*Conformational comparison of hexasaccharide **(1)** in the unbound and S1-RBD-bound states.* Conformationally sensitive three-bond proton-proton ($^3J_{H-H}$) coupling constants confirmed the $^4C_1$ chair conformation of glucosamine and glucuronic acid residues (**Table S2b**). In contrast, the conformation of the IdoA residue is in equilibrium between $^4C_1$, $^1C_4$ and $^2S_0$ forms, the position of which depends on the identity and sulfation status of the neighbouring residues. The population of each conformer, estimated from the $^3J_{H-H}$ coupling constants; $^3J_{H1-H2}$ and $^3J_{H4-H5}$ of the IdoA2S (residue

10.1002/chem.202202599

F) were <1 Hz and 1.9 Hz, respectively, indicating the prevalence of $^1C_4$ conformers, in agreement with Ferro *et al*. [31, 32]. In contrast, for IdoA2S (residue B), the complete set of $^3J_{HH}$ values indicated an equilibrium between $^1C_4$ and $^2S_0$ conformations of 63:37 (**Table S2b**). These findings were confirmed by comparing the NOEs for the free ligand and trNOEs with the bound ligand, providing evidence of the interaction and forming a description of the intra-residue and inter-glycosidic conformational changes upon binding (**Figure S4**). The cross-relaxation rates vary considerably when the ligand is bound to the protein, even though both NOEs and trNOEs remain positive, with consequent large variation in the cross-peak intensities upon interaction between ligand and protein (**Table S2c, S2d** and **S2e**).

As expected from previous studies of protein-bound heparin oligosaccharides, the conformation of GlcNS6S (residues E, C and A) and GlcA (residue D) of **(1)** bound to S1-RBD was $^4C_1$,[33] confirmed by strong trNOEs between diaxial H3 and H5 protons (not shown), and the fitting of theoretical and experimental trNOEs (see below).

Since IdoA2S in $^1C_4$ and $^2S_0$ conformations exhibits distinct H5–H2 distances (4.0 and 2.4 Å respectively), the ratio between the magnitudes of experimental H5-H2 and H5-H4 NOEs qualitatively provides the proportions of the two conformers. The weak H5-H2 NOE of IdoA2S (residue F) is compatible with almost pure $^1C_4$ conformation (H5-H2/H5-H4 ratio 0.1), while the stronger H5-H2 NOEs measured for IdoA2S (residue B) conforms to an equilibrium between $^1C_4$ and $^2S_0$ conformations (H5-H2/H5-H4 ratio 0.4) (**Table S2d**), in agreement with $^3J_{HH}$ measurements. The line-broadening observed in the spectrum of **(1)**-S1-RBD complex precluded the measurement of coupling constants and therefore, the conformation of iduronic acid residues was obtained by interpretation of the trNOEs. Unexpectedly, neither IdoA2S residue (residues F and B) exhibited significant changes in their average conformation, since H2-H5/H4-H5 trNOE ratios of IdoA2S (residue F) and IdoA2S (residue B) remained unchanged (**Table S2d**).

The oligosaccharide backbone conformation in unbound and bound state with S1-RBD was described by the set of inter-glycosidic NOEs and trNOEs (**Table S2e**). Although, the top rotor dynamic of heparin oligosaccharides longer than four residues, does introduce a dependency of the NOE cross relaxation rates on the orientation of H-H vectors with the molecular axis, the effect can be considered negligible in this case. The ratios between the *linewidth (half height width)* of H1 signals in the unbound and bound states of residues F to A are approximately uniform (0.75, 0.80, 0.79, 0.78, 0.74, 0.65 respectively), indicating only a weak anisotropic effect. Even though the comparison between NOEs and trNOEs cannot be precisely correlated with a change of distance upon binding, evidence of significant conformational changes could be underlined. Docking and MD simulation showed minor changes of the inter-glycosidic geometries, presumably indicating an adaptation of the backbone conformation to the surface of S1-RBD to optimize contacts. The most significant change concerns the GlcA (residue D)-GlcNS6S (residue C) glycosidic linkage, which is also observed experimentally by the significant variation of H1-H6/ H1-H4 NOE ratios that changes from 0.6 to 0.3 between the unbound and bound states (**Table S2e**), other values remaining broadly unchanged.

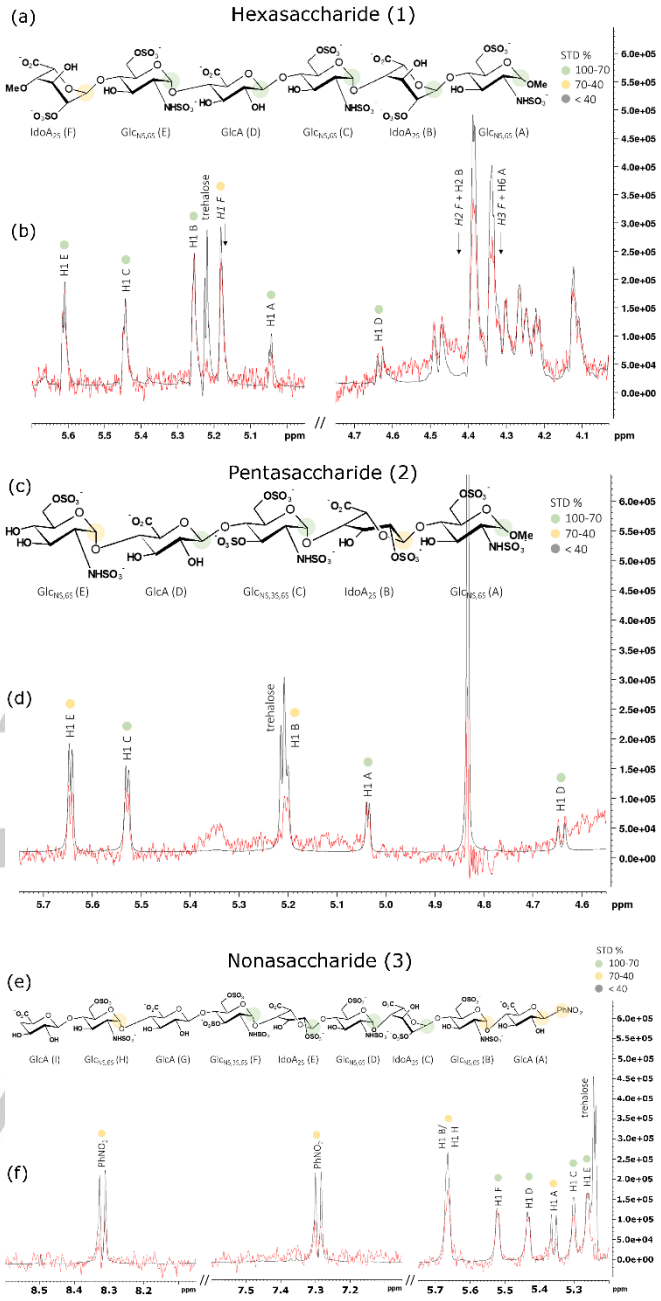

Figure 3. Oligosaccharide (1) (2) and (3) interactions with S1-RBD described by ^{1}H-STD NMR spectra in D_2O. (a). Sequence representation of **(1)** and regions interacting with S1-RBD. (b). Partial ^{1}H-STD NMR spectrum of the **(1)**-S1-RBD complex (red) superimposed on the corresponding reference spectrum (black). (c). Representation of the sequence and of the interacting regions of **(2)** in the **(2)**-S1-RBD complex. (d). Partial ^{1}H-STD NMR spectrum of the **(2)**-S1-RBD complex (red) superimposed on the corresponding reference spectrum (black). (e) Representation of the sequence and the interacting regions of **(3)** in the **(3)**-S1-RBD complex. (f). Partial ^{1}H-STD NMR spectrum of the **(3)**-S1-RBD complex (red) superimposed on the corresponding reference spectrum (black).

*Molecular modelling of the binding mode of hexasaccharide **(1)** with S1-RBD.*

Analysis of the S1-RBD surface allowed detection of three putative sites.[17] Site I is defined by amino acid residues: R346, N354, K356, R357, R355, K444 and R466, while sites II and III include K424, R454, R457, K458, K462, R466, and R403, R408, K417, K444 respectively. Notably, site III (distinct from site I and II) partially overlaps the ACE2 binding site and, while it may

engage HS initially, it can probably be excluded from the S1-RBD complex that recognizes ACE2 on the basis that S1-RBD binds ACE2 in the presence of heparin or HS.[22] In this study, these putative binding sites were ranked by a hybrid docking/MD simulation approach, using **(1)** as a 'molecular probe'.

Molecular docking simulations were used in the first stage to generate three principal solution sets (clusters) of geometries (poses) of the **(1)**-S1-RBD complex, that were obtained separately (independently) targeting site I, site II, or site III. In a second stage, the MD simulation allowed the geometry of these clusters to be refined and their Poisson Boltzmann free energy of binding (ΔG_{PB}^{bind}, molecular mechanic Poisson Boltzmann Surface Area approximation, MMPBSA) to be calculated. The 'per-residue' decomposition of the ΔG_{PB}^{bind} term allowed quantification of the contribution of each residue to ΔG_{PB}^{bind}. In the third stage, selected geometries of the complex comprising **(1)**-S1-RBD were validated by comparison between simulated and experimental intra-residue and inter-glycosidic trNOEs. The results of stage one and two are summarized in **Table 1**.

The selected docking solutions were ranked according to the AutoDock score function (ADT), the cluster population (2nd and 3rd columns) and the binding free energy ΔG_{PB}^{bind} (6th column). **Table 1** suggests that **(1)** preferentially binds site I of S1-RBD in comparison to sites II and III, evident by comparison of the ADT and the free energy of binding indicators. **Table 1** also shows that, while sites II and III present comparable binding energies, in terms of the population of the docked complexes, **(1)** preferentially binds site II over site III. Below, the interactions of **(1)** with S1-RBD are analysed in terms of sites I, II and III according to the docking/MD simulation results, considering the most representative solutions and the 'per residue' contribution to the free energy of binding.

*Evidence for hexasaccharide **(1)** binding site I of the S1-RBD in two binding modes*.

Regarding interactions between **(1)** and site I of the S1-RBD, three initial sets of docking solutions emerged, represented by clusters 1, 2 and 3 (**Table 1**), that are characterized by comparable (lowest) free energies of binding, and correspond to the most favourable molecular recognition (**Table 1**, 6th column). The 3D structure analysis reveals that clusters 1 and 2 are nearly superimposable (in terms of contacts and free energy of binding), cluster 2 cannot be distinguished from cluster 1 (RMSD $((\mathbf{1}))_{cluster1} - ((\mathbf{1}))_{cluster2} = 3.2$ Å), so they will be treated together. Interestingly, **(1)**-S1-RBD complexes that belong to cluster 1 and cluster 3 present opposite orientations of **(1)** in relation to S1-RBD, despite their comparable binding energies. In cluster 1, hexasaccharide **(1)** orients its non-reducing end towards the ACE2 binding site (we term this binding mode A), while in cluster 3, it binds S1-RBD in the opposite orientation (binding mode B).

The corresponding complexes (**Figure 4**) have also been analysed in terms of their residue-wise free energy of binding ΔG_{PB}^{bind}. While some key residues - R346, K355, R356, R357 - contribute to the binding interaction in both modes A and B, mode A presents a stronger contribution from R346 (-11 vs -6 Kcal mol^{-1}) and weaker involvement of R466 (-2 vs -11 Kcal mol^{-1}). Moreover, binding mode B shows more efficient contact through N354 than mode A (-3 vs 1.3 Kcal mol^{-1}), while, mode B presents stronger repulsive contributions at GlcA (residue D), GlcNS6S (residue C) and D398, than binding mode A (5.8, 4.3, and 3 Kcal mol^{-1} vs 1.7, 2.9 and 1.9 Kcal mol^{-1}). Finally, in binding mode A, S1-RBD interacts more efficiently with **(1)** through residues: N450, Y451, R454, R457, K458 and K462, located near site II (**Figure 4**).

Further analysis of the unfavourable contributions of **(1)**, shows that GlcA (residue D) and GlcNS6S (residue C) present strong positive de-solvation energies (ΔG_{sol}) that, for some contacts, are not counterbalanced by favourable (negative) electrostatic and/or van der Waals terms (**Table S3**). At the molecular level, the positive values of $\Delta G_{PB}^{bind}(i)$ at GlcA (residue D) and GlcNS6S (residue C) in binding mode A (*1.7 and 2.9 Kcal* mol^{-1}, respectively) correlated with a de-solvation penalty when GlcA approaches S1-RBD surface at the backbone of K355, and the N-sulfo group of GlcNS6S becomes proximal to the hydrophobic side chain of I468 upon binding. In both contacts, the solvation shell surrounding the ligand is locally lost upon binding. A similar analysis can be applied when **(1)** interacts with the S1-RBD in binding mode B. In this case, the carboxyl group of GlcA loses its solvation shell, being oriented toward the surface of the S1-RBD (near Cα of N354), without an electrostatic interaction to compensate this loss of energy. Analogously, GlcNS6S (residue C) presents unfavourable contacts localized on its ring and on the 6-O-sulfate group ($\Delta G_{PB}^{bind}(i)$ = *3.0* and *2.0 Kcal* mol^{-1}, respectively); while only the N-sulfate group presents favourable contacts with R355 and R466 ($\Delta G_{PB}^{bind}(i)$ = *-0.8*). The contribution of GlcNS6S (residue C) to the free energy of binding is therefore unfavourable ($\Delta G_{PB}^{bind}(GlcNS6S(C))$ = *5.80* Kcal mol^{-1}) (**Table S3**).

*Hybrid docking-MD simulations and interpretation of trNOEs suggest that hexasaccharide **(1)** binds S1-RBD (site I) in two binding modes.*

The glycosidic conformation of **(1)** in the bound state with S1-RBD considering both binding modes A and B, as predicted by the hybrid docking-MD simulation, and summarized in **Table 1**, is further described by Ramachandran plots (**Figure 5**) The CORCEMA selected structures (black empty circles in **Figure 5**), support the most populated states ϕ_i/ψ_i sampled by MD simulation of the complexes formed when **(1)** binds S1-RBD in modes A and B. The agreement between the CORCEMA selected structure of the **(1)**-S1-RBD complex and intra-residue and inter-glycosidic trNOEs is summarized in **Table S4** and **S6**, interestingly, this agreement improves when both A and B modes have been considered, as can be observed comparing the R-factor values. Interestingly, the MD simulation predicts for IdoA2S (residue B) a $^2S_0$ and $^1C_4$ conformation when **(1)** binds S1-RBD in mode A and B, respectively, further supporting the improvement of the fitting between experimental and theoretical trNOEs when the **(1)**-S1-RBD complex involves both A and B modes (**Table S4**)

*Hexasaccharide **(1)** binds site II and III of the S1-RBD less efficiently than site I*.

The 3D structure analysis of the S1-RBD shows that both sites II and III present exposed positive patches, but their binding to **(1)** is significantly weaker. Analysis of the molecular binding interactions in the bound state with S1-RBD involving sites II and III is reported in **Figure S5** and **Figure S6**, respectively. As for site I, the interaction between **(1)** and site II of S1-RBD is described by two possible complexes, labelled as clusters 1 and 2 of the corresponding docking simulation (**Table 1**). As for site I, clusters 1 and 2 of site II present opposite orientations of **(1)**. Docking solution cluster 1 is characterized by the non-reducing end of **(1)** oriented toward the S1 trimer, while the opposite

10.1002/chem.202202599

orientation is found in cluster 2, (**Figure S5 b** and **d**, respectively). The per-residue analysis of the free energy of binding corresponding to clusters 1 and 2, shows that the efficiency by which **(1)** binds site II of S1-RBD is lower than site I, despite the orientation. The docking/MD simulation procedure applied to the interaction of **(1)** with site III of S1-RBD, indicated putative binding regions that partially interfere with the recognition site of ACE2 (**Figure S6**). The corresponding binding free energy (ΔG_{PB}^{bind} = *-12.1(3)*) is comparable with the poses that involve site II, but is weaker than site I (**Table 1**). The histogram of ΔG_{PB}^{bind} *(i)* of this complex shows that residues of site III contribute less strongly to the interaction than to site I (comparing **Figure S6 a** with **Figure 4 c** and **d**). A more detailed description of the favourable and unfavourable contributions to the interaction of sites II and III is summarized in **Figure S5** and **Figure S6**.

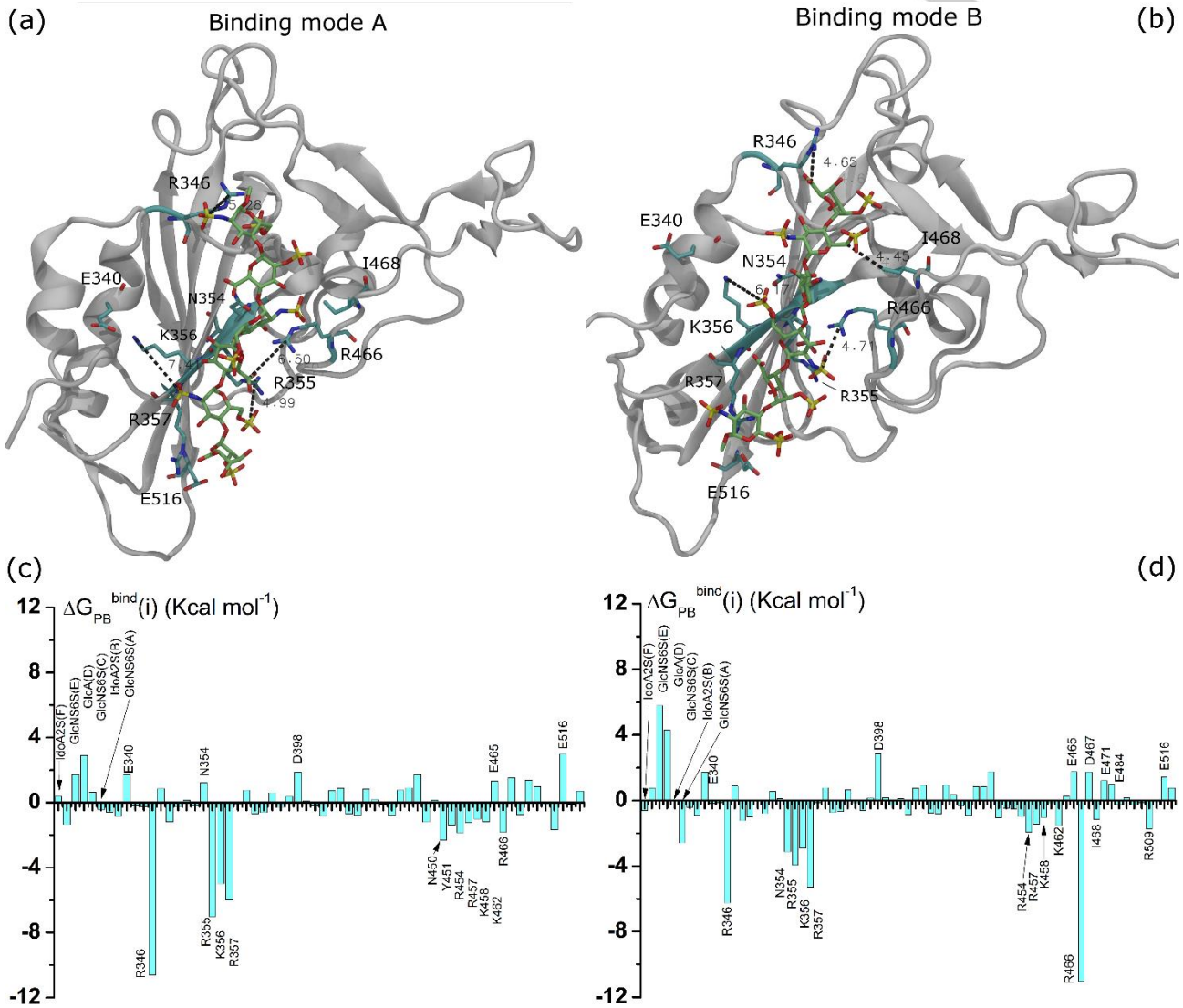

Figure 4. Analysis of the interactions between hexasaccharide (1) and the S1-RBD of SARS-CoV-2 (site I) in binding modes A and B. Binding mode 'A' is characterised by the oligosaccharide reducing end oriented toward the ACE2 site; mode 'B' by the oligosaccharide with its reducing end oriented opposite the ACE2 site. (a). The 3D structure of the **(1)**-S1-RBD complex sampled by MD simulation (simulation time 81.58 ns) and binding the S1-RBD in mode A. (b). The 3D structure of the **(1)**-S1-RBD complex sampled by MD simulation (simulation time 37.75 ns) and binding the S1-RBD in mode B. (c) and (d). The histograms of the residue wise contribution to the Poisson Boltzmann free energy of binding ΔG_{PB}^{bind} (i) of the complex (1)-S1-RBD in binding modes A and B, respectively. In panels a and b, the S1-RBD is represented by grey ribbon; amino acids of site I are underlined by cyan ribbon; **(1)** is represented by green, red and blue tubes indicating carbon, oxygen and nitrogen atom, respectively. Selected contact distances are underlined by dashed segments; distances are reported in Angstroms. In panels c and d, the histograms are averaged at the production stage of the MD simulation trajectory (**Table 1**). Energies are in Kcal mol^{-1} units.

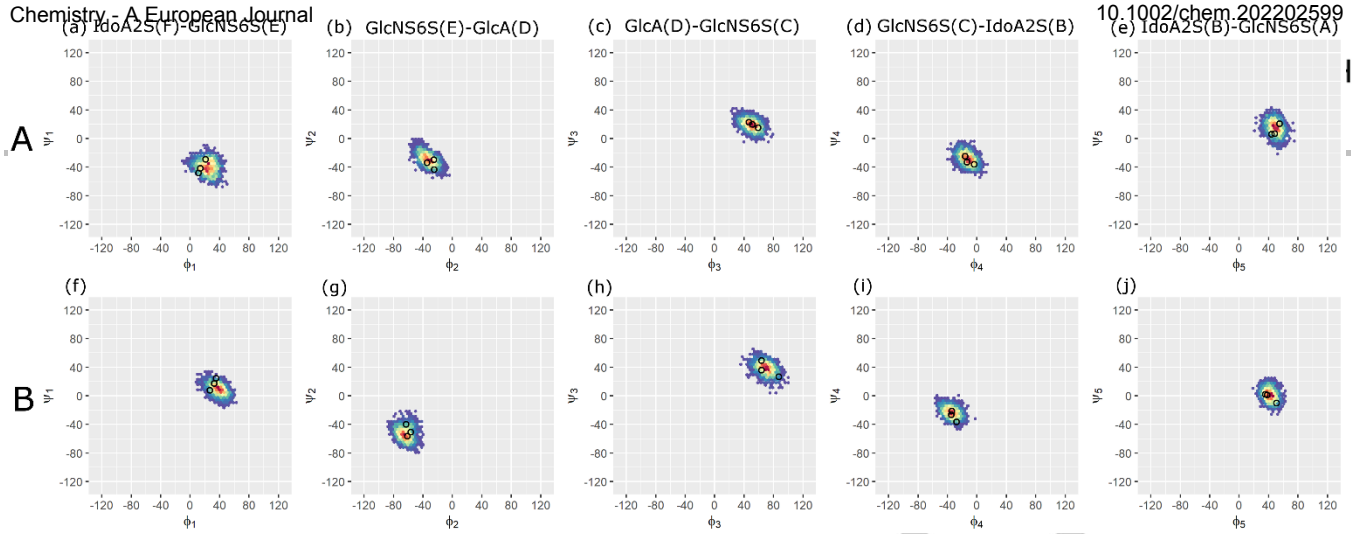

Figure 5. Conformational analysis of binding modes A and B, of hexasaccharide (1) to the S1-RBD. Ramachandran plots of the glycosidic dihedral angles ϕ_i/ψ_i of **(1)** in bound state with S1-RBD (site I). Two possible orientations of **(1)** bound to the S1-RBD are represented, corresponding to binding modes A and B. Binding mode A, is characterized by the non-reducing end of **(1)** oriented toward the ACE2 recognition site (panels a to e); binding mode B, in which **(1)** is opposite to the ACE2 site (panels f to j). The glycosidic dihedral states are sampled by MD simulation in the production stage intervals: 80 to 100 ns (mode A) and 36 to 56 ns (mode B). A density colour map is superposed on each Ramachandran plot. The colour gradient (blue to red) is proportional to the density of the sampled states ϕ_i/ψ_i, and qualitatively predicts the preferred conformation of each glycosidic linkage. The empty circles indicate the values of ϕ_i/ψ_i for the three selected pairs of **(1)**-S1-RBD complex which interpret the experimental trNOEs (**Table S6**).

These theoretical descriptions collectively suggest that sites II and III of S1-RBD recognize and bind **(1)** less efficiently than site I, despite comparable numbers of solvent accessible Lys and Arg residues. The less homogeneous distribution of positively charged patches present on the surface of sites II and III, frequently interrupted by negatively charged Asp, and/or Glu residues, may explain this finding. Positively charged side chains could be at least partially 'neutralized', if surrounded by the carboxyl groups of Asp and Glu residues. The result is a decrease in efficiency by which site I of S1-RBD binds **(1)**. This is clearly visible in **Figure 4 a** and **b**, in which the domain of positively charged patches formed by R346, R355, K356, R357 and R466 is not interrupted by Asp or Glu residues and the nearest carboxyl group belongs to E340, E516, outside of site I. This is not the case for sites II and III (**Figure S5 b** and **d**, and **Figure S6 b**). In fact, in site II E465, D467 and E471 are distributed between the positive patches of R466, K462, R454, R457 and K458, weakening their binding to **(1)**. Analogously, in site III D420 and D405 are in proximity of R408 and R403, again disturbing the ability of site III to efficiently bind **(1)**. Extrapolating the hexasaccharide **(1)** into a hypothetical polysaccharide at binding site I indicates that positively charged areas are encountered (**Figure 6 a**), which are distinct from those more negatively charged areas, containing Asp or Glu residues, unfavourable for binding indicated in sites II (**Figure 6 b**) and III (**Figure 6 c**). This implies that, in the polysaccharide case, site I is likely to be more favoured than site II or III.

*Hybrid docking-MD simulations and interpretation of ^{1}H-STD NMR values show that pentasaccharide **(2)** also binds site I of S1-RBD in two binding modes.*

The interaction between **(2)** and S1-RBD (site I) was further investigated by the hybrid docking/MD simulation. As for hexasaccharide **(1)**, pentasaccharide **(2)** binds S1-RBD using two distinct modes (**Table S5**). In docking solution cluster 1, the saccharide **(2)** orients its non-reducing end toward the ACE2 binding site (mode A), while in cluster 2, it binds S1-RBD in the opposite orientation (mode B).

The interaction involves the set of residues: R346, N354, R355, K356, R357 and R466 that characterize site I of S1-RBD in binding modes A and B, as for **(1)**. A detailed analysis of this interaction is reported in **Figure S7 a** and **c**. Interestingly, unlike **(1)**, **(2)** is predicted to bind S1-RBD preferentially in mode B, supported (*in silico*) by ΔG_{PB}^{bind} and by several unfavourable contacts localized on the glucosamines (residues E, C and A) when **(2)** binds S1-RBD in mode A (**Table S5** and **Figure S7 a**). The ^{1}H-STD NMR signal of H6 in **Figure S8** supports binding mode B, where the H6 of GlcNS3S6S (residue C) is oriented to the surface of S1-RBD within 4 Å of the carbonyl group of R355 (**Figure S9**). Despite that, the coexistence of the ^{1}H-STD NMR signals of the HN and H6 of GlcNS3S6S (residue C), that show comparable intensity when **(2)** interacts with S1-RBD in water (**Figure S10 c**), does not exclude the possibility that **(2)** bind S1-RBD in both A and B modes, in this molecular recognition event.

Discussion and conclusions

Heparan sulfate, the anionic, high molecular weight linear polysaccharide component of cell surfaces and extracellular matrix associated proteoglycans is highly variable in structure. Its expression tracks evolutionary development and complexity in animals [35]. One role is to maintain and regulate complex mechanical and signalling networks through manifold protein interactions, [36, 37] which exhibit varied structural selectivity for the sugar. Claims of highly specific oligosaccharide sequences binding proteins are often made. These usually depend on the selection of highly charged species that were found using affinity methods employing electrolyte elution. This biases the selection in favour of charged species. This problem is often compounded by the initial search for binding oligosaccharides being made from oligosaccharide populations that contain only limited structural diversity compared to the huge number that are potentially available. [36]

Those attempts that have searched for HS saccharide binding partners among diverse structures [38-40], have shown that each protein recognises a subset of sugar structures to different extents and, that these may overlap. Moreover, some binding structures lack activity, e.g. in dual-receptor systems. [15], while a single saccharide may bind a protein in several distinct modes. Most of the studies leading to this conclusion have involved mammalian proteins but, few comparable investigations have been made of the interactions of viral proteins with HS.

The nature and extent of this specificity lies at the heart of the mechanism employed by viruses to achieve the species, tissue and cell tropism required to ensure their propagation. Viruses, like

other microbiological pathogens, have evolved to employ the evolutionarily conserved HS, as an initial means of host cell identification and attachment. The extent of specificity and selectivity of HS structural features is a delicate balance for the pathogen. Excessive specificity limits successful binding events, hence, subsequent infection, while excessive laxity would entail widespread binding, much of which could be unproductive. Furthermore, multiple binding sites on a protein and/or high affinity for HS could restrict protein diffusion. [38-40] Thus, affinity and avidity are tuned to enable a virus to access receptors near the cell surface. Influenza virus achieves this by means of a glycosidase, [44] but is absent from SARS-CoV-2. Instead, HS is proposed to serve as the first attachment point for the S protein, whereby virions can travel from the external to the internal layers of the glycocalyx using this low affinity (potentially multivalent) initial contact, until the specific S1-RBD-ACE2 is engaged at the cell surface but, this proposal requires a mechanistic and molecular basis.

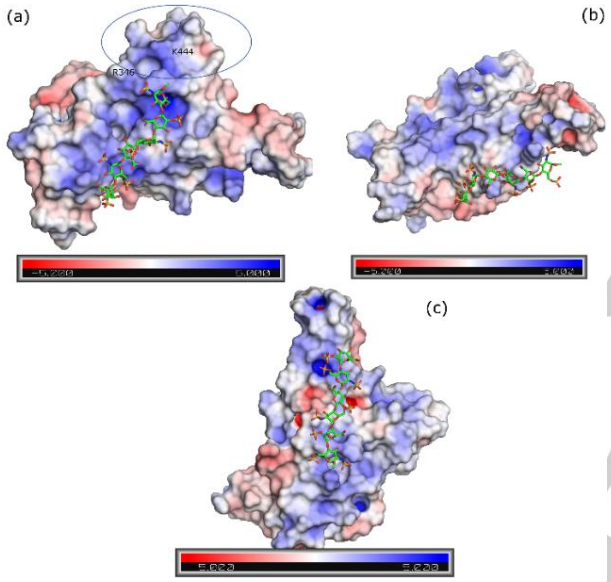

Figure 6. Electrostatic potential maps of the S1-RBD surface with hexasaccharide (1) in the bound state at site I (a), site II (b), or site III (c). The gradient of electrostatic potential (units KT e^{-1}) increases from red (negative) to blue (positive). The complex of **(1)** with the S1-RBD was sampled by MD simulation at 81.58, 44, and 44 ns, and corresponds to the poses reported in **Figures 4a**, **S4b** and **S4b**. Extrapolating the binding saccharide further across the protein surface indicates that in site I (a), an area of positive charge is encountered, containing residues R346 and K444, while in site II, an area of negative charge is encountered (b).

For ligand probes **(1)** and **(2)**, several modes of binding to site I were explored, without a strong preference emerging. Interestingly, the two modes involved opposite saccharide orientation and revealed no detectable changes in the conformation of L-IdoA2S residues, or of the glycosidic linkage geometries that might enable tighter binding. More precisely, experimental data supports involvement of the previously identified amino acids, R346, N354, R355, K356, R357, R466, and K444 (representing the core of site I) [19] [20], as the principal site for interaction, leaving the flexible loops of S1-RBD free to engage ACE2 (**Figure 7**). The simulated intra-residue and inter-glycosidic trNOEs of **(1)** in interaction with S1-RBD in average agreed better with experiment when at least two (A and B) binding modes were considered. The longer glycan **(3)** enabled estimation of the minimum GAG length that continuously binds S1-RBD, agreeing with that of the shortest probes of this investigation (**Figure 3**). This is the first time that *in-silico* HS-S1-RBD binding models have been validated using experimental NMR interaction data, suggesting that the HS-S1-RBD interaction lacks high structural selectivity and binding specificity.

These results can be interpreted mechanistically; HS serving as an initial virus binding target, providing a loosely bound tether, attachment to which both constrains the virion and activates the spike protein, thereby enhancing the possibility of initial contact (and much more specific interaction) with ACE2.

Oligosaccharide probes identify the energetically most favoured binding sites on the protein surface and the most significant contributions to binding energy originate in charge-charge interactions, extending over relatively long distances, and enabling some topological obstacles on the protein surface to be overcome. As in previous studies of interactions between fibroblast growth factors and heparin/HS, [37, 38] the amino acid residues involved most likely represent a core binding region.

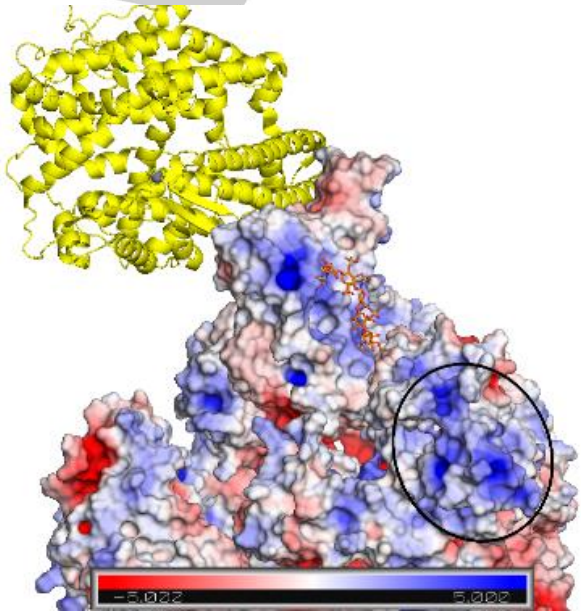

Figure 7. Hexasaccharide (1) bound to site I, modelled into a hypothetical macromolecular complex does not interfere with molecular recognition between S1-RBD and ACE2 and reveals contiguous areas consistent with the binding of heparan sulfate polysaccharide. The macromolecular complex superimposes **(1)**-S1-RBD complex sampled by MD simulation and supported by trNOEs (**Figure 4** a) on the S1-RBD subunit of the trimeric protein S (PDB ID 6VYB), matching the Cα backbone between residues 333 and 526 (RMSD = 0.88 Å). The ACE2-S1-RBD (PDB ID 6M0J) complex is represented by yellow ribbon, superimposed on the S1-RBD of the trimeric S protein, matching the Cα backbone between residues 333 and 526 (RMSD = 0.67 Å). The electrostatic potential (in units KT e^{-1}) of the protein surface is represented by colour gradient from red (negative) to blue (positive). **(1)** is drawn in orange, blue, red, and yellow coloured tubes, indicating carbon, nitrogen, oxygen and sulfur atoms, respectively. Extrapolation of the core binding region, identified by docking of the **(1)**, to longer HS chains from the top (S1-RBD) or bottom (S1) of **(1)**, encounters regions of positive charge (blue patches), likely to favour binding of the polysaccharide.

Extending the hexasaccharide in site I from either end to form a hypothetical polysaccharide encounters adjacent positive regions

on the S1-RBD surface (**Figure 6a**) which, when incorporated into a spike protein-RBD complex model, indicates contiguous areas of positive charge (**Figure 7**) consistent with binding longer HS chains across S1. Furthermore, HS binding does not interfere in interactions between S1-RBD loops and ACE2.

The multiplicity of binding modes exhibited by several structures, while indicating broad tissue recognition and enhancing initial viral attachment, supports a dynamic interaction of S1-RBD with cellular and extracellular matrix HS, which prevents the virus becoming locally 'trapped' and unable to diffuse to cell surface ACE2. This has implications for the design of potential inhibitors; highly specific inhibitors would not be optimal against manifold low specificity interactions and suggests that structurally diverse compounds, characterised by high affinity towards S1 and including multidentate inhibitors, should be considered. Moreover, a highly specific inhibitor would provide selective pressure favouring binding site mutations which, combined with extant alternative HS binding areas on the S1-subunit surface, make it relatively easy for the virus to mutate around. This is consonant with reports that spike S1-RBD binds diverse HS-like oligosaccharides [22], synthetic linear or branched polyanions, i.e. polyglycerol sulfate, [45] and the inhibition of viral attachment to cells by HS-like structures. [13, 17, 46] A further interesting class, characterized by hybrid poly-anionic/hydrophobic structure, such as pixatimod (PG545), interferes with the ACE2 binding site, inhibiting SARS-CoV-2 on Vero E6 and human cells [47].

Cell surface HS is vital to a broad range of fundamental biological processes in the host, a fact that many pathogenic organisms exploit, while the host is unable to evolve to evade this fundamental dependency. Thus, SARS CoV-2 joins a growing list of pathogens that exploits cell surface HS as initial, low-specificity points of contact and attachment that enable the infectious process to begin.

Experimental Section

Experimental details are reported in Supporting information sections.

Acknowledgements

We gratefully acknowledge ITALFARMACO S.p.A. for sponsoring this research. We acknowledge the HPC team of CINECA (Consortium for High-Performance Computing, Casalecchio di Reno Bologna, Italy) for computing resources and support. We acknowledge Prof. J Liu (University of North Carolina) to deliver us the oligosaccharide **(3)**.

Keywords: SARS-CoV-2 • Protein S spike • Heparan sulfate • NMR spectroscopy • MD simulation

[1] E. Hartenian, D. Nandakumar, A. Lari, M. Ly, M. J. Tucker, B. A. Glaunsinger, *J. Biol. Chem*. **2020**, *295*, 12910–12934.
[2] Coronaviridae Study Group of the International Committee on Taxonomy of V., *Nat. Microbiol.* **2020**, *5*, 536–544.
[3] F. Zhou, T. Yu, R. Du, D. Ronghui, G. Fan, Y. Liu, Z. Liu, J. Xiang, Y. Wang, B. Song, X. Gu, L. Guan, Y. Wei, H. Li, X. Wu, J. Xu, S. Tu, Y. Zhang, H. Chen, B. Cao, *Lancet* **2020**, *395*, 1054–1062.
[4] F. A. Klok, M. J. H. A. Kruip, N. J. M. van der Meer, M. S. Arbous, D. A. M. P. J. Gommers, K. M. Kant, F. H. J. Kaptein, J. van Paassen, M. A. M. Stals, M. V. Huisman, H. Endeman, *Thromb Res* **2020**, *191* 145-147.h
[5] D. B. Kell, G. J. Laubsche, E. Pretorius. *Biochem J.* **2022**, *479*, 537-559.
[6] M. Gui, W. Song, H. Zhou, J. Xu, S. Chen, Y. Xiang, X. Wang, *Cell Res.* **2017**, *27*, 119-129.
[7] T. Sztain, S.-H. Ahn, A. T. Bogetti, L. Casalino, J. A. Goldsmith, E. Seitz, R. S. McCool, F. L. Kearns, F. Acosta-Reyes, S. Maji, G. Mashayekhi, J. A. McCammon, A. Ourmazd, J. Frank, S. J. McLellan, L. T. Chong, R. E. Amaro, *Nat. Chem.* **2021** *13*, 963–968.
[8] W. Li, M. J. Moore, N. Vasilieva, J. Sui, S. K. Wong, M. A. Berne, M. Somasundaran, J. L. Sullivan, K. Luzuriaga, T. C. Greenough, H. Choe, M. Farzan, *Nature*, **2003**, *426*, 450-454.
[9] J. Lan, J. Ge, J. Yu, S. Shan, H. Zhou, S. Fan, Q. Zhang, X. Shi, Q. Wang, L. Zhang, X. Wang, *Nature*, **2020**, *581*, 215–220.
[10] M. Hoffmann, H. Kleine-Weber, S. Schroeder, N. Krüger, T. Herrler, S. Erichsen, T. S. Schiergens, G. Herrler, N. H. Wu, A. Nitsche, M. A. Müller, C. Drosten, S. Pöhlmann, *Cell*, **2020**, *181*, 1–10.
[11] Q. Zhang, C. Z. Chen, M. Swaroop, M. Xu, L. Wang, J. Lee, A. Q. Wang, M. Pradhan, N. Hagen, L. Chen, M. Shen, L. Z. Luo, X. Xu, Y. Xu, W. Huang, W. Zheng, Y. Ye, *Cell Discovery* **2020**, *6*, 80.
[12] T. M. Clausen, D. R. Sandoval, C. B. Spliid, J. Pihl, H. R. Perrett, C. D. Painter, A. Narayanan, S. A. Majowicz, E. M. Kwong, R. N. McVicar, B. E. Thacker, C. A. Glass, Z. Yang, J. L. Torres, G. J. Golden, P. L. Bartels, R. N. Porell, A. F. Garretson, L. Laubach, J. Feldman, X. Yin, Y. Pu, B. M. Hauser, T. M. Caradonna, B. P. Kellman,C. Martino, P. L. S. M. Gordts, S. K. Chanda, A. G. Schmidt, K. Godula, S. L. Leibel, J. Jose, K. D. Corbett, A. B. Ward, A. F. Carlin, J. D. Esko, *Cell* **2020**, 183, 1043−1057.
[13] C. A. de Haan, Z. Li, E. te Lintelo, B. J. Bosch, B. J. Haijema, P. J. Rottier, *J. Virol*. **2005**, *79*,14451–14456.
[14] A. Milewska, M. Zarebski, P. Nowak, K. Stozek, J. Potempa, K. Pyrc, *J. Virol*., **2014**, *88*, 13221–13230.
[15] a) A. Krufka, S. Guimond, A. C. Rapraeger, *Biochemistry* **1996**, 35, 11131–11141; b) C. Lanzi, G. Cassinelli *Biochem Pharmacol.* **2020**, *178*:114084. doi: 10.1016/j.bcp.2020.114084.
[16] C. J. Mycroft-West, D. Su, S. Elli, Y. Li, S. Guimond, G. Miller, J. Turnbull, E. Yates, M. Guerrini, D. Fernig, M. Lima, M. Skidmore, *Biorxiv*, https://doi.org/10.1101/2020.02.29.971093.
[17] C. J. Mycroft-West, D. Su, I. Pagani, T. R. Rudd, S.Elli, N. S. Gandhi, S. E. Guimond, G. J. Miller, M. C. Z. Meneghetti, H. B. Nader, Y. Li, Q. M. Nunes, P. Procter, N. Mancini, M. Clementi, A. Bisio, N. R. Forsyth, V. Ferro, J. E. Turnbull, M. Guerrini, D. G. Fernig, E. Vicenzi, E. A. Yates, M. A. Lima, M. A. Skidmore, *Thromb Haemostasis* **2020**; *120*, 1700–1715.
[18] S. Y. Kim, W. Jin, A. Sood, D. W. Montgomery, O. C. Grant, M. M. Fuster, L. Fu, S. J. Dordick, R. J. Woods, F. Zhang, R. J. Linhardt, *Antivir. Res*., **2020**, *181*, 104873.
[19] S. H. Kim, F. L. Kearns, M. A. Rosenfeld, L. Casalino, M. J. Papanikolas, S. Simmerling, R. E. Amaro, R. Freeman, *ACS Cent. Sci.* **2022**, *8*, 22–42.
[20] G. Paiardi, S. Richter, P. Oreste, C. Urbinati, M. Rusnati, R. C. Wade, *J. Biol. Chem.*, **2022**, *298*, 101507.
[21] J. E. Chittum, N. V. Sankaranarayanan, C. P. O'Hara, U. R. Desai, *ACS Med. Chem. Lett*. **2021**, *12*, 1710−1717.
[22] L. Liu, P. Chopra, X. Li, K. M. Bouwman, S. M. Tompkins, M. A. Wolfert, R. P. de Vries, G.-J. Boons, *ACS Cent. Sci.* **2021**, *7*, 1009−1018.
[23] D. Idrees, V. Kumar, *Biochem. Bioph. Res Co*. **2021**, *554*, 94-98.
[24] Z. P. Schuurs, E. Hammond, S. Elli, T. R. Rudd, C. J. Mycroft-West, M. A. Lima, M. A. Skidmore, R. Karlsson, Y.-H. Chen , I. Bagdonaite, Z. Yang, Y. A. Ahmed, D. J. Richard, J. Turnbull, V. Ferro, D. R. Coombe, N.S. Gandhi, *Comp. and Struct. Biotech. J.*, **2021**, *19*, 2806–2818.
[25] D. Wrapp, N. Wang, K. S. Corbett, J. A. Goldsmith, C.-L. Hsieh, O. Abiona, B. S. Graham, J. S. McLellan, *Science* **2020**, *367*, 1260–1263.
[26] A. Yu, A. J. Pak, P. He, V. Monje-Galvan, L. Casalino, Z. Gaieb, A. C. Dommer, R. E. Amaro, G. A. Voth, *Biophys. J.* **2021**, *120*, 281-292.
[27] M. A. Tortorici, D. Veesler, *Adv. Virus Res* **2019**, *105*, 93–116.
[28] A. C. Walls, Y.-J. Park, M. A. Tortorici, A. Wall, A. T. McGuire, D. Veesler, *Cell* **2020**, *181*, 281-292.
[29] Y. Yuan, D. Cao, Y. Zhang, J. Ma, J. Qi, Q. Wang, G. Lu, Y. Wu, J. Yan, Y. Shi, X. Zhang, G. F. Gao, *Nat Commun.* **2017**, *8*, 15092.
[30] G. Torri, B. Casu, G. Gatti, M. Petitou, J. Choay, J.C. Jacquinet, P. Sinai. *Biochem. Biophys. Res. Commun*. **1985**, *128*, 134.

[31] M. Hricovlni, G. Torri *Carbohydr. Res.* **1995**, 268, 159-175
[32] D. R. Ferro, A. Provasoli, M. Ragazzi, B. Casu, G. Torri, V. Bossennec, B. Perly, P. Sinay, M. Petitou, J. Choay, *Carbohydr. Res*., **1990**, *195*, 157–167.
[33] D. R. Ferro, A. Provasoli, M. Ragazzi, G. Torri, B. Casu, G. Gatti, J. C. Jacquinet, P. Sinay, M. Petitou, J. Choay, *J. Am. Chem. Soc.* **1986**, *108*, 6773 – 6778.
[34] M. Guerrini, S. Guglieri, B. Casu, G. Torri, P. Mourier, C. Boudier, C. Viskov, *J. Biol. Chem*. **2008**, *283*, 26662–26675.
[35] A. Ori, M. C. Wilkinson, D. G. Fernig, *J. Biol. Chem.,* **2011**, *286*, 19892–19904.
[36] A. Ori, M. C. Wilkinson, D. G. Fernig, *Front. Biosci*. *(Landmark Ed)* **2008**, *13*, 4309–4338.
[37] Q. M. Nunes,D. Su, P. J. Brownridge, D. M. Simpson, C. Sun, Y. Li, T. P. Bui, X. Zhang, W. Huang, D. J. Rigden, R. J. Beynon, R. Sutton, D. G. Fernig, *PLoS ONE*, **2019**, *14*, e0217633.
[38] M. H. Howard, T. Cenizal, S. Gutteridge, W. S. Hanna, Y. Tao, M. Totrov, V. A. Wittenbach, Y.-J. Zheng, *J. Med. Chem.* **2004**, *47*, 6669-6672.
[39] R. Xu, A. Or, T. R. Rudd, K. A. Uniewicz, Y. A. Ahmed, S. E. Guimond, M. A. Skidmore, G. Siligardi, E. A. Yates, D. G. Fernig, *J. Biol. Chem.* **2012**, 287, *47*, 40061–40073.
[40] Y. Li, C. Sun, E. A. Yates, C. Jiang, M. C. Wilkinson, D. G. Fernig, *Open Biol.* **2016**, *6*, 150275.
[41] L. Duchesne, V. Octeau, R. N. Bearon, A. Beckett, I. A. Prior, L. Brahim, D. G. Fernig, *PloS Biol.*, **2012**, *10*, e1001361.
[42] C. Sun, M. Marcello, Y. Li, D. Mason, R. Lévy, D. G. Fernig, *Open Biol.* **2016**, *6*, 150277.
[43] E. Migliorini, D. Thakar, J. Kuühnle, R. Sadir, D. P. Dyer, Y. Li, C. Sun, B. F. Volkman, T. M. Handel, L. Coche-Guerente, D. G. Fernig, H. Lortat-Jacob, R. P. Richter, *Open Biol*. **2015**, *5*, 150046.
[44] M. D. Vahey, D. A. Fletcher, *eLife* **2019**, *8*, 43764 doi: 10.7554/eLife.43764
[45] C. Nie, P. Pouyan, D. Lauster, J. Trimpert, Y. Kerkhoff, G. P. Szekeres, M. Wallert, S. Block, A. K. Sahoo, J. Dernedde, K. Pagel, B. B. Kaufer, R. R. Netz, M. Ballauff, R. Haag, *Angew. Chem. Int. Ed*. **2021**, *60*, 15870–15878.
[46] J. A. Tree, J. E. Turnbull, K. R. Buttigieg, M. J. Elmore, N. Coombes, J. Hogwood, C. J. Mycroft-West, M. A. Lima, M. A. Skidmore, R. Karlsson, Y.-H. Chen, Z. Yang, C. M. Spalluto, K. J. Staples, E. A. Yates, E. Gray, D. Singh, T. Wilkinson, C. P. Page, M. W. Carroll, *Br J Pharmacol*. **2021**, *178*, 626–635.
[47] S. E. Guimond, C. J. Mycroft-West, N. S. Gandhi, J. A. Tree, T. T. Le, C. M. Spalluto, M. V. Humbert, K. R. Buttigieg, N. Coombes, M. J. Elmore, M. Wand, K. Nyström, J. Said, Y. X. Setoh, A. A. Amarilla, N. Modhiran, J. D. J. Sng, M. Chhabra, P. R. Young, D. J. Rawle, M. A. Lima, E. A. Yates, R. Karlsson, R. L. Miller, Y.-H. Chen, I. Bagdonaite, Z. Yang, J. Stewart, D. Nguyen, S. Laidlaw, E. Hammond, K. Dredge, T. M. A. Wilkinson, D. Watterson, A. A. Khromykh, A. Suhrbier, M. W. Carroll, E. Trybala, T. Bergström, V. Ferro, M. A. Skidmore, J. E. Turnbull, *ACS Cent. Sci*, **2022**, *8*, 527-545.

10.1002/chem.202202599

WILEY-VCH

RESEARCH ARTICLE

Entry for the Table of Contents

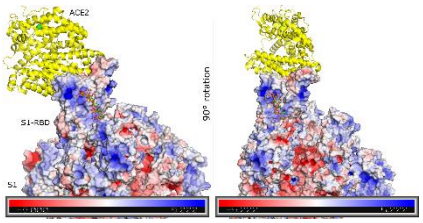

Hexasaccharide **(1)** bound to site I in binding mode A and B (orange and green tubes), shows that multiple binding modes between heparan sulfate (HS) and S1 (electrostatic potential map on the surface) are allowed; the hypothetical macromolecular complex HS-S1 does not interfere with the interaction involving S1-RBD and ACE2, supporting the co-receptor role of HS in the activation of the SARS-CoV-2 S protein.